AGU PUBLICATIONS

JGR

Journal of Geophysical Research: Atmospheres

RESEARCH ARTICLE

10.1002/2017JD027355

GPM Satellite Radar Measurements of Precipitation and Freezing Level in Atmospheric Rivers: Comparison With Ground-Based Radars and Reanalyses

Forest Cannon[1], **F. Martin Ralph**[1], **Anna M. Wilson**[1], **and Dennis P. Lettenmaier**[2]

[1]Center for Western Weather and Water Extremes, Scripps Institution of Oceanography, University of California, San Diego, La Jolla, CA, USA, [2]Department of Geography, University of California, Los Angeles, CA, USA

Key Points:

- Precipitation in atmospheric rivers accounts for nearly 10% more oceanic precipitation in satellite radar estimates than reanalyses
- Over the eastern North Pacific Ocean, 25% of satellite radar-derived precipitation rates exceed the 99th percentile of reanalyses
- Satellite radar freezing level height estimates agree exceptionally well with ground-based radar observations and reanalyses

Correspondence to:
F. Cannon,
fcannon@ucsd.edu

Citation:
Cannon, F., Ralph, F. M., Wilson, A. M., & Lettenmaier, D. P. (2017). GPM satellite radar measurements of precipitation and freezing level in atmospheric rivers: Comparison with ground-based radars and reanalyses. *Journal of Geophysical Research: Atmospheres*, *122*, 12,747–12,764. https://doi.org/10.1002/2017JD027355

Received 5 JUL 2017
Accepted 17 NOV 2017
Accepted article online 27 NOV 2017
Published online 14 DEC 2017

Abstract Atmospheric rivers (ARs) account for more than 90% of the total meridional water vapor flux in midlatitudes, and 25–50% of the annual precipitation in the coastal western United States. In this study, reflectivity profiles from the Global Precipitation Measurement Dual-Frequency Precipitation Radar (GPM-DPR) are used to evaluate precipitation and temperature characteristics of ARs over the western coast of North America and the eastern North Pacific Ocean. Evaluation of GPM-DPR bright-band height using a network of ground-based vertically pointing radars along the West Coast demonstrated exceptional agreement, and comparison with freezing level height from reanalyses over the eastern North Pacific Ocean also consistently agreed, indicating that GPM-DPR can be used to independently validate freezing level in models. However, precipitation comparison with gridded observations across the western United States indicated deficiencies in GPM-DPR's ability to reproduce the spatial distribution of winter precipitation, likely related to sampling frequency. Over the geographically homogeneous oceanic portion of the domain, sampling frequency was not problematic, and significant differences in the frequency and intensity of precipitation between GPM-DPR and reanalyses highlighted biases in both satellite-observed and modeled AR precipitation. Reanalyses precipitation rates below the minimum sensitivity of GPM-DPR accounted for a 20% increase in total precipitation, and 25% of radar-derived precipitation rates were greater than the 99th percentile precipitation rate in reanalyses. Due to differences in the proportions of precipitation in convective, stratiform bright-band, and non-bright-band conditions, AR conditions contributed nearly 10% more to total precipitation in GPM-DPR than reanalyses.

1. Introduction

Atmospheric rivers (ARs) are a key component of the global water budget that account for a major fraction of precipitation over midlatitude oceans and coastlines, including the U.S. West Coast (e.g., Dettinger, 2013; Gimeno et al., 2014; Kingston et al., 2016; Lavers & Villarini, 2013; Ralph et al., 2017, 2004; Viale & Nuñez, 2011; Zhu & Newell, 1998). Despite the importance of ARs to global moisture fluxes and regional water resources, understanding and forecasting these features remains a challenge due in part to their formation and propagation over the ocean, where in situ and ground-based observations are extremely limited. One of the more promising recent technological developments that could help fill this data gap is the launch of the Global Precipitation Measurement Mission (GPM) satellite (Hou et al., 2014; Skofronick-Jackson et al., 2016), which carries a Dual-Frequency Precipitation Radar (DPR) that helps monitor global precipitation between 65°N and 65°S. This monitoring includes precipitation rate estimation, snow versus rain discrimination, freezing level height estimation, and discernment of convective versus stratiform precipitation types (Iguchi et al., 2010).

However, the ability of GPM to fill gaps in AR measurements offshore, and over the western United States, has yet to be evaluated. This study uses a unique set of observations and methodologies to evaluate the Dual-Frequency Precipitation Radar (DPR) on board GPM, including a network of ground-based precipitation profiling radars that regularly monitor snow-level aloft in precipitation (White et al., 2013) and a state-of-the-art AR detection method (Rutz et al., 2014), completely independent of GPM. The paper also evaluates the ability of GPM-DPR measurements to accurately represent the regional climatology of precipitation across major portions of the U.S. West Coastal states, and over the Pacific Ocean to its west. And, finally, it compares the GPM-derived climatology of precipitation in the region in terms of rain rates to that provided by a modern reanalysis data set (Modern-Era Retrospective Analysis for Research Application, version 2, MERRA-2) to search for potential differences. This study is motivated by the following issues:

1. Precipitation is a key term in the water vapor budget within ARs and yet is poorly observed over the oceans (L'Ecuyer et al., 2015).
2. The altitude of the freezing level is a key factor in determining precipitation impacts on landfall, including mountain snowpack formation/depletion, streamflow, and flooding (Neiman et al., 2014; White et al., 2010), yet is poorly observed ahead of AR landfall.
3. Model predictions of AR landfall, precipitation amounts, and freezing level contain serious errors (Ralph et al., 2010, 2016) that might be reduced by better initialization.
4. GPM offers an opportunity to help fill these gaps in AR monitoring, and yet quantitative evaluations of GPM-DPR performance in measuring precipitation and freezing level in ARs are not available.
5. Although it is known that GPM-DPR is limited in its ability to measure light rain rates (Iguchi et al., 2010), and that global models produce excessive light rain and drizzle (Stephens et al., 2010), comparisons of these two key sources of precipitation information have not been conducted for AR environments.

In this study, GPM-DPR along-track reflectivity profiles were evaluated over the West Coast and eastern North Pacific Ocean. GPM was launched in February 2014, following the success of the Tropical Rainfall Measurement Mission (TRMM; Huffman et al., 2007). A key sensor on board TRMM was the Ku band precipitation radar (PR), which measured three-dimensional reflectivity of precipitation droplets in the atmosphere. GPM-DPR exceeds TRMM PR's capabilities by utilizing differential attenuation between a similar Ku band (13.6 GHz) sensor and an additional Ka band (35.5 GHz) radar to provide information on drop size distributions and precipitation intensity that improve precipitation rate and freezing level estimates. This information additionally enables the discernment of precipitation type and microphysics (Hamada & Takaybu, 2016; Iguchi et al., 2010), which describe various cloud particle formation, growth, and precipitation processes, depending on altitude and environmental conditions (e.g., Martner et al., 2008; Matrosov, 2007, 2013). Previously, Matrosov (2013) employed a W band radar (~94 GHz) on board the CloudSat satellite (CloudSat CPR; Stephens et al. 2002) to investigate precipitation processes within ARs over the eastern North Pacific Ocean over a 3 year period (2007–2009). While the methodology for analyzing ARs over the ocean in the present study is similar to that of Matrosov (2013), it is important to note that CloudSat CPR-based findings are likely to differ from GPM-DPR results based on differences in each radar's minimum sensitivity.

The present study provides novel analyses of GPM-DPR measurements in atmospheric rivers and discusses the benefits and limitations of applying GPM-DPR to observing precipitation processes over the western United States and eastern North Pacific Ocean. Despite notable caveats, it is shown that GPM-DPR improves observation of AR precipitation and freezing level over the data sparse oceans and that these measurements are useful for evaluating the simulation of ARs by global models. Differences in precipitation frequency and intensity between GPM-DPR and reanalyses are highlighted by discrepancies of nearly 10% in the contribution of ARs to total precipitation over the eastern North Pacific Ocean, while comparisons of freezing level demonstrate remarkable agreement in height and variability.

2. Data and Methodology

2.1. Satellite Precipitation Radar

This research utilized the GPM-DPR standard level 2 (L2) product, version 04 (2ADPR; Iguchi et al., 2010), from the matched beam scan swath. Radar reflectivity in three dimensions, precipitation rate, bright-band height, and precipitation type variables were evaluated (listed in the GPM 2ADPR file structure documentation as, "zFactorCorrected," "precipRateESurface," "heightBB," and "typePrecip," respectively). The reflectivity data used have a vertical bin sampling of 125 m (176 vertical bins) and a horizontal resolution of ~5.2 km. The along-track horizontal footprint of the Ka and Ku band matched scan swath is ~125 km (25 horizontal bins in the along-track direction). Only data from the five cross-track bins closest to the nadir-pointing ray at the center of the swath were used on account of increasing surface clutter with increasing distance from nadir (Kubota et al., 2016), and in order to avoid sampling precipitation features at an angle, which bias both precipitation and bright-band retrievals (Hamada & Takaybu, 2016; Hirose et al., 2012). GPM completes roughly 16 orbits per day between 65°N and 65°S, and the 2ADPR product has a latency of less than 24 h.

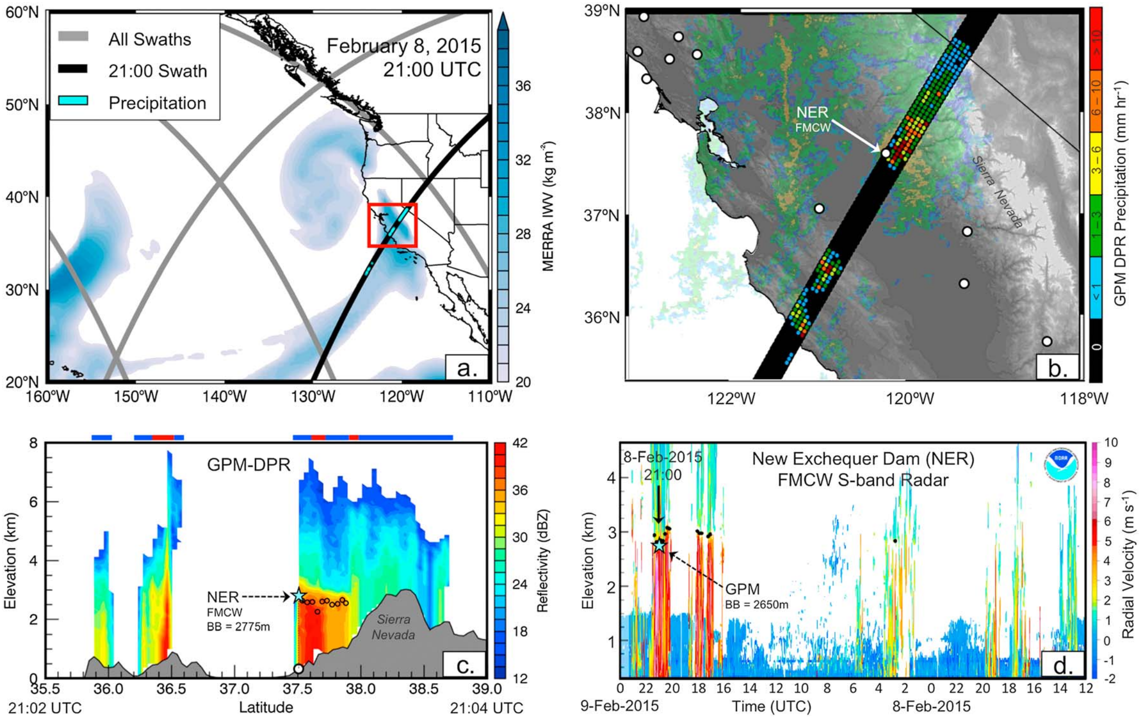

Figure 1. (a) Example GPM-DPR swaths during an AR on 8 February 2015. (b) A subset of the domain (red box) over Central California is shown in the center panel with NEXRAD reflectivity over topography. The full swath is shown in black, with colored dots indicating measured precipitation rates at individual GPM-DPR bins. White dots indicate vertically profiling radars. (c) The vertical profile of GPM-DPR reflectivity from the Ka band and topography along the center of the swath over California. Black circles indicate the identified bright-band height and colored bars above the plot indicate stratiform (blue) and convective (red) precipitation identification by GPM-DPR. (d) The FMCW S band radar measured radial velocity provided by NOAA ESRL Physical Sciences Division.

The study period spanned three winter seasons (October through March; 2014–2017), focusing on the period of the year during which ARs routinely make landfall in California. The study domain covers the eastern North Pacific Ocean and western North America (160°W–110°W; 20°N–60°N) (Figure 1a).

GPM satellite tracks recorded during an AR event impacting California on 8 February 2015 demonstrate the challenges presented by the satellite's sampling frequency (Figure 1a). Integrated water vapor (IWV) from reanalysis (described in section 2.4) indicates the location of the AR feature of interest. In this example, GPM made an overpass of landfalling AR conditions (elongated region of IWV $>$ 20 mm) in Central California at approximately 21:05 UTC. Only 5 of GPM's 16 daily orbits passed through the study domain on the day that the AR made landfall, 2 of which sampled some portion of the AR, and only 1 of which sampled the event over the west coast. The limited track frequency and narrow swath width illustrate that large areas of the domain are unsampled during any given event and that it is relatively rare for GPM-DPR to sample an AR during landfall. However, a single AR propagating across the Pacific over several days (this particular AR propagated for approximately 7 days) is likely to be sampled multiple times by the near-polar orbiting satellite.

Along-track GPM-DPR precipitation estimates from the five angle bins that were used in this study are plotted over composite reflectivity at 21:05 UTC from the National Weather Service's Next-Generation Weather Radars (NEXRAD) to illustrate the data sampling methodology (Figure 1b). Local precipitation maxima were observed by both GPM-DPR and NEXRAD over the coastal ranges and foothills of the Sierra Nevada Mountains, indicating strong spatial agreement between observations. An example reflectivity profile from the center bin of the Ka band from Figure 1b is also plotted over topography (Figure 1c). Additional GPM-DPR variables (e.g., precipitation rate and type, and bright-band height) that were evaluated in this study were derived from reflectivity by the algorithms described in the GPM-DPR theoretical basis document (Iguchi et al., 2010) and Awaka et al. (2016). Comparison of GPM-DPR precipitation characteristics with ground-based observations are discussed in section 3. Figure 1d is included to demonstrate the use of a

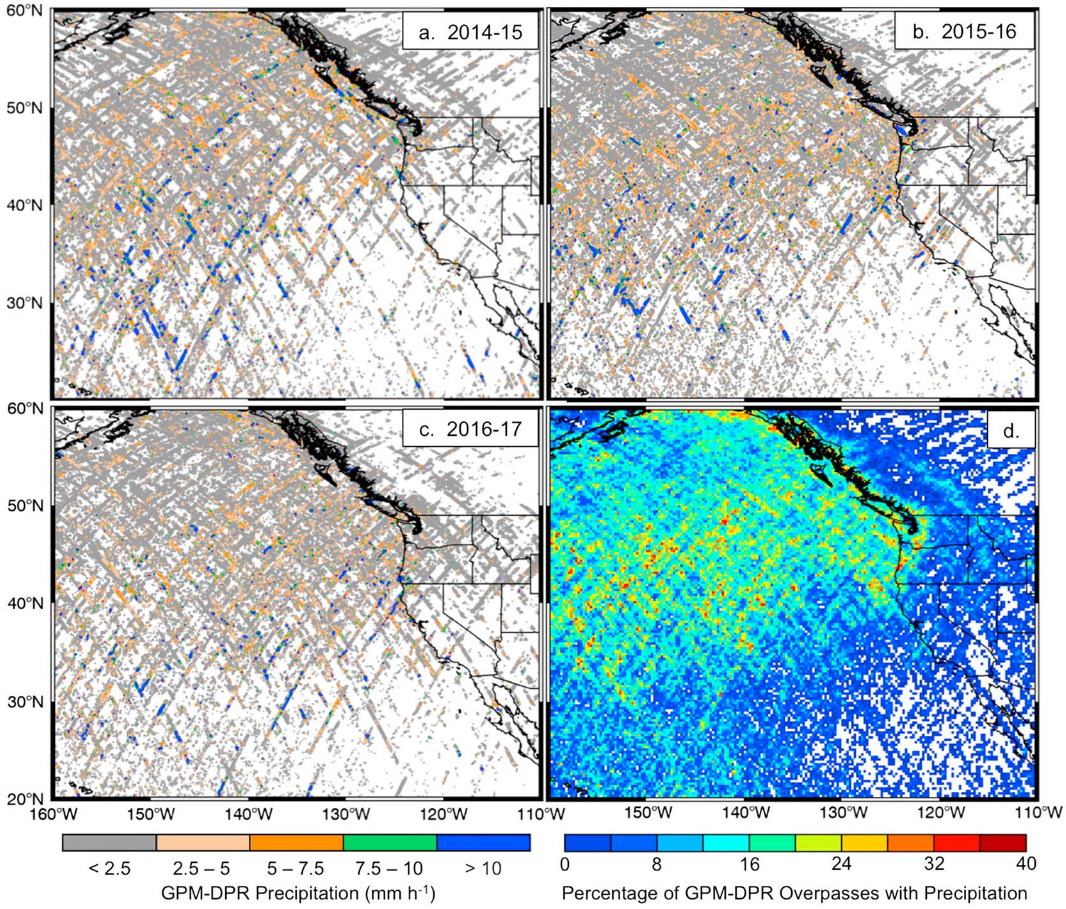

Figure 2. All GPM-DPR overpasses, with individual bins color coded by measured precipitation rate, are shown for the (a) 2014–2015, (b) 2015–2016, and (c) 2016–2017 winter seasons, and (d) the percentage of all winter overpasses that measured precipitation, within 0.25° grid boxes.

unique network of vertically profiling radars to validate GPM-DPR bright-band measurements (discussed in section 2.3).

The location of all GPM-DPR precipitation retrievals within the study domain for each winter season is shown in Figures 2a–2c. Swaths are vertically stacked and color coded according to precipitation rate. It is notable that there were relatively few precipitation retrievals along the West Coast in all years, with the minimum occurring during the exceptionally dry 2014–2015 winter season (California Department of Water Resources, 2016). The percentage of overpasses that recorded precipitation over the entire study period (Figure 2d) indicates that precipitation retrievals were most frequent along the coastal ranges of western Canada, Washington, and Oregon (>25% of overpasses), and moderately frequent in the North Pacific above 30°N (10–25% of overpasses). GPM-DPR had the lowest precipitation sampling frequency over a large region of semipermanent high pressure in the southeast portion of the domain, including Southern California. These figures reflect the regional precipitation climatology (Adler et al., 2003) and are useful for understanding the spatial variability of GPM-DPR sampling-related issues, which complicate comparisons of the satellite product with in situ measurements and reanalyses.

2.2. In Situ Precipitation

GPM-DPR precipitation rates were compared with colocated precipitation data from the Parameter Regression on Independent Slopes Method (PRISM; Daly et al., 1994), which is an interpolated precipitation product with daily temporal and 4 km horizontal resolution. PRISM daily resolution data are not optimal for comparison with GPM-DPR, given the instantaneous sampling of the satellite; however, the improved spatial coverage afforded by interpolation made considerably more comparisons possible than with individual stations. Rather than compare absolute precipitation amounts, bulk statistics of the spatial patterns of normalized precipitation during the winter season were evaluated. Comparison with GPM-DPR along-track precipitation retrievals was achieved by sampling the single PRISM grid point whose centroid was nearest the center bin of the GPM swath on the date of overpass.

2.3. Ground-Based Snow-Level Radars

GPM-DPR bright-band height, based on a reflectivity peak in the Ku band, and the slope of differential reflectivity between the Ka band and Ku band, within a 3 km vertical range centered 1 km below model-estimated freezing level elevation (Iguchi et al., 2010; Le & Chandrasekar, 2013b), was validated using a unique network of 27 ground-based vertically pointing radars across California, Oregon, and Washington (Neiman et al., 2014; White et al., 2013). This network includes S band radars (3 GHz), Frequency-Modulated Continuous Wave radars (FMCW), and wind profiling radars (449 MHz and 915 MHz) that were developed and are maintained by the National Oceanic and Atmospheric Administration's Physical Science Division (NOAA ESRL-PSD) (ftp://ftp1.esrl.noaa.gov/psd2/data/realtime//). This unique observing network is described in White et al. (2013). White et al. (2002) describe the methodology for automated bright-band retrievals from radars operating in the 400–4000 MHz frequency range, which gives the scientific basis for the publicly available bright-band height data in the NOAA PSD archive. Estimation is based on identification of a peak in signal-to-noise ratio (equivalent to reflectivity) and increasing Doppler vertical velocity, indicating the increased fall speed of rain compared to snow (White et al., 2002). Each ground-based radar considered has hourly to subhourly temporal resolution overlapping some portion of the study period. An example time series of the vertical structure of radial velocity and snow level measurements from the New Exechequer Dam FMCW radar is shown for the 8 February 2015 AR event (Figure 1d). The FMCW radar measured a bright-band at ~2,775 m at the time of GPM's overpass, while the DPR measured a bright-band at ~2,650 m in the bin corresponding to the FMCW site. Although the melting layer typically has a width of several hundred meters, due to the noninstantaneous melting of ice hydrometeors, the ground-based profiling radars identify bright-band heights as the reflectivity maxima within this layer, typically near its center (White et al., 2002). GPM-DPR's bright-band height similarly refers to the peak of Ku band reflectivity and/or the peak of the differential reflectivity slope within the melting layer (Le & Chandrasekar, 2013b).

2.4. Reanalysis

This research used NASA Modern-Era Retrospective Analysis for Research Application, version 2 (MERRA-2) (Molod et al., 2015; Rienecker et al., 2011). MERRA-2, integrated at a resolution of 0.67° longitude by 0.5° latitude with 72 Lagrangian vertical levels, was chosen on account of its refined representation of the atmosphere's hydrological cycle (Rienecker et al., 2011) and its high spatiotemporal resolution, which minimized inconsistencies in comparisons with instantaneous GPM-DPR retrievals. Bias-corrected time-averaged precipitation at 1 h temporal resolution, and instantaneous temperature and geopotential height, interpolated to 42 pressure levels, at 3 h temporal resolution were evaluated. Freezing-level elevations were calculated for each 3 h snapshot by reverse-interpolating the temperature and geopotential height profiles at each horizontal grid point and subsequently identifying the geopotential height at the 0°C isotherm within that grid point (Harris et al., 2000). In the case of multiple 0°C levels in a single vertical profile, due to inversions, only the lowest level was retained. Comparison with GPM along-track retrievals was achieved by sampling the single MERRA-2 grid point whose centroid was nearest the center of the GPM swath, at the nearest time slice in the 1-hourly precipitation and 3-hourly temperature data sets. MERRA's improved simulation of the hydrological cycle relies on assimilating precipitation estimates, including those from the GPM microwave imager. However, the GPM-DPR measurements evaluated here are not assimilated and are independent.

3. GPM-DPR In Situ Validation

3.1. Precipitation

Before applying GPM-DPR to study AR precipitation characteristics over the ocean, the sensor was evaluated over the western United States, where ARs contribute significantly to annual precipitation and ample in situ data are available for validation. Although precipitation processes and instrument challenges (e.g., ground clutter) are different between ocean and land portions of the study domain, this comparison highlights important considerations regarding GPM-DPR's performance in representing regional precipitation patterns with a relatively short period of accumulated data. There have been several field campaigns and comprehensive validation experiments, such as the Olympic Mountains Experiment (OLYMPEX; Houze et al., 2017), that

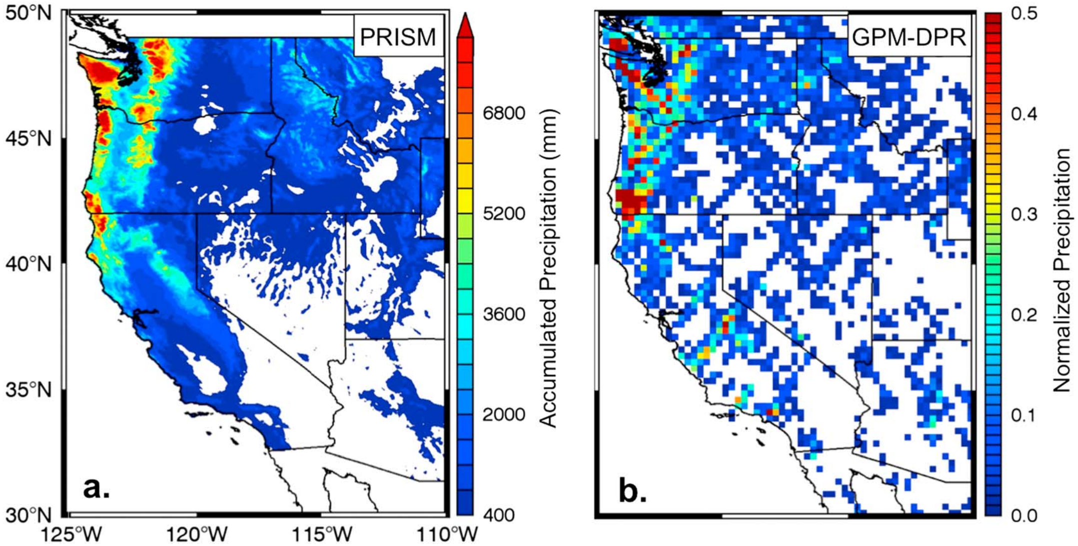

Figure 3. (a) Accumulated PRISM precipitation during the 2014–2017 winter seasons study period. (b) The spatially normalized sum of GPM-DPR instantaneous precipitation rates for all overpasses during the study period, within 0.25° grid boxes. Data were normalized by the domain maximum and minimum values to emphasize spatial gradients.

have specifically focused on quantifying the performance of GPM-DPR instrumentation and algorithms in measuring reflectivity and deriving related precipitation products. The comparisons presented here are based on spatiotemporal sampling over multiple seasons and are intended to illustrate how low-sampling frequency affects subsequent analyses, rather than as an evaluation of instrumentation or algorithm performance.

Total accumulated PRISM precipitation during the study period demonstrates the characteristic pattern of orographic enhancement over the western United States (Dettinger et al., 2004; Roe, 2005), indicated by steep precipitation gradients across the Coast Ranges, Cascade Mountains, and Sierra Nevada Mountains (Figure 3a). Additionally, there is a climatological north-south precipitation gradient (Daly et al., 1994) that was particularly pronounced over the study period due to below average precipitation in California during the 2014/2015 and 2015/2016 winter seasons (He et al., 2017). Figure 3b demonstrates the ability of GPM-DPR to reproduce PRISM's salient precipitation patterns. The plotted data show the normalized sum of GPM-DPR precipitation measurements from all overpasses during the study period, binned to 0.25° resolution on account of sparsity (outside of the Pacific Northwest, there are no individual 0.25° grid points with more than 10 GPM overpasses that recorded precipitation during the study period). Here normalization focuses the comparison on spatial precipitation patterns rather than absolute values.

The pattern of orographic enhancement observed in PRISM (Figure 3a) is degraded in the GPM-DPR plot (Figure 3b), primarily due to insufficient sampling (Figure 2). The spatial correlation between Figure 2b and PRISM, resampled to 0.25° resolution (not shown), is 0.65. GPM-DPR's results were best in western Oregon and Washington, where frequent precipitation was observed. Given the small sample size for locations in Southern and Central California, where precipitation events are less frequent, and the variability of instantaneous precipitation rates during events is large, GPM-DPR did not produce a statistically robust precipitation climatology for this region. Increasing the number of cross-track bins used in the analyses from 5 to 11 improves the spatial correlation with PRISM to 0.7 and slightly improved the qualitative representation of orographic precipitation gradients (not shown). Despite the moderate improvement gained through increased cross-track sampling, this research employed only five cross-track bins to minimize the impact of known issues in precipitation and bright-band height estimation in off-nadir bins (Hirose et al., 2012; Kubota et al., 2016), which would unnecessarily introduce uncertainty into further analyses.

The hypothesis that differences were attributable to sampling deficiency and not measurement or algorithm error is further supported by previous analyses from the OLYMPEX experiment, which demonstrated that airborne instrumentation and algorithms similar to those developed for GPM-DPR are ideally suited to measure orographic precipitation processes (Houze et al., 2017). Additionally, GPM-DPR's predecessor,

Table 1
The Principal Characteristics of the Vertically Pointing Radars That Provide Bright-Band Height Measurements—Name, Coordinates, Altitude, Profiling Frequency, Installation Date, and Project Name

ID	Name	Latitude	Longitude	Elevation (m)	Instrument	Install	Project
1	Forks	47.97	−124.40	95	449 MHz wind profiler	7/21/2015	DOE
2	Astoria	46.15	−123.88	3	449 MHz wind profiler	3/9/2015	DOE
3	Troutdale	45.55	−122.39	12	915 MHz wind profiler	8/26/2015	DOE
3[a]	Troutdale[a]	45.55	−122.39	12	3 GHz precipitation profiler	12/2/2015	DOE
4	Wasco	45.59	−120.67	462	915 MHz wind profiler	9/2/2015	DOE
5	Boardman	45.82	−119.81	107	915 MHz wind profiler	10/5/2015	DOE
6	Condon	45.24	−120.17	891	915 MHz wind profiler	10/8/2015	DOE
7	Prineville	44.29	−120.90	959	915 MHz wind profiler	8/5/2015	DOE
8	North Bend	43.42	−124.24	5	449 MHz wind profiler	10/15/2015	DOE
9	Happy Camp	41.79	−123.38	366	FMCW precipitation profiler	2/2/2012	HTW
10	Shasta Dam	40.72	−122.43	202	FMCW precipitation profiler	12/9/2009	HTW
11	Chico	39.70	−121.91	42	915 MHz wind profiler	6/2/2000	HTW
12	Oroville	39.53	−121.49	114	FMCW precipitation profiler	12/8/2011	HTW
13	Colfax	39.08	−120.94	644	FMCW precipitation profiler	12/10/2008	HTW
14	New Exchequer	37.60	−120.27	259	FMCW precipitation profiler	12/3/2010	HTW
15	Pine Flat Dam	36.83	−119.33	184	FMCW precipitation profiler	12/2/2010	HTW
16	Visalia	36.31	−119.39	81	915 MHz wind profiler	3/17/2010	HTW
17	Kernville	35.75	−118.42	816	FMCW precipitation profiler	1/2/2012	HTW
18	San Bernardino	34.20	−117.34	602	FMCW precipitation profiler	3/12/2013	HTW
19	Santa Barbara	34.43	−119.85	2	449 MHz wind profiler	1/20/2016	HTW
20	San Luis Res.	37.06	−121.07	81	FMCW precipitation profiler	4/2/2013	HTW
21	Saint Helena	38.55	−122.49	135	FMCW precipitation profiler	7/9/2014	HTW
22	Middletown	38.75	−122.71	972	3 GHz precipitation profiler	12/10/2014	HTW
23	Santa Rosa	38.51	−122.80	32	3 GHz precipitation profiler	10/7/2014	SCWA
24	Bodega Bay	38.32	−123.07	15	449 MHz wind profiler	3/22/2013	HTW
25	Cazadero	38.61	−123.22	478	3 GHz precipitation profiler	11/11/2004	HTW
26	Hopland	39.00	−123.09	253	3 GHz precipitation profiler	10/22/2015	HTW
27	McKinleyville	40.97	−124.11	56	449 MHz wind profiler	11/18/2015	HTW

Note. The ID numbers correspond to the map in Figure 4a.
[a]DOE = Department of Energy; HTW = NOAA Hydrometeorological test bed—West; CWA = Sonoma County water agency.

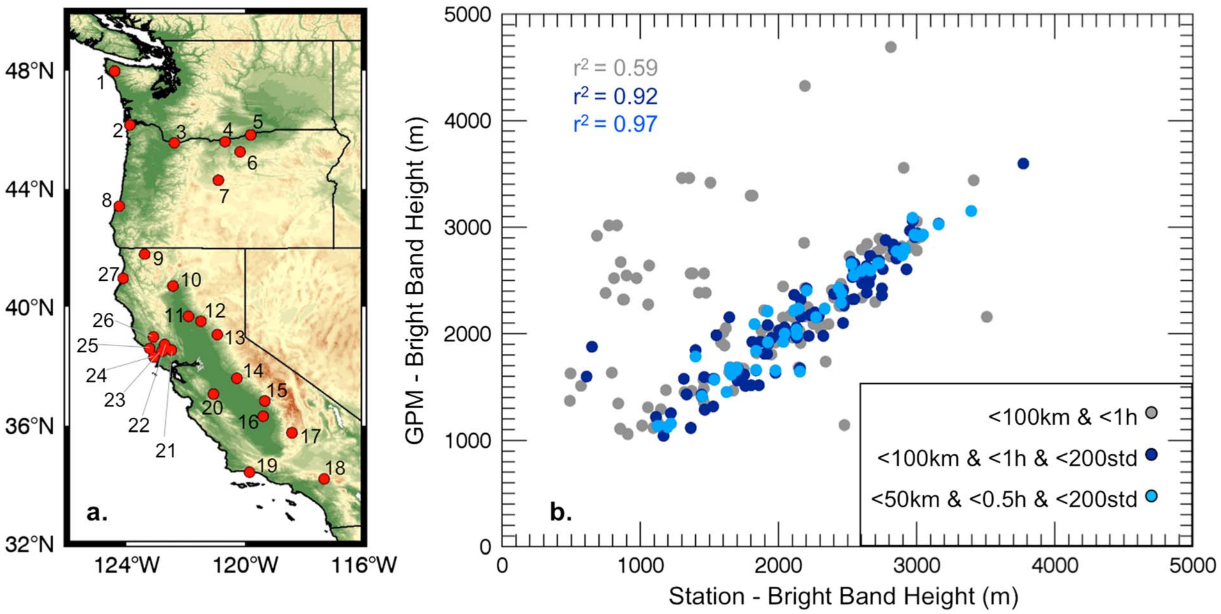

Figure 4. (a) Locations of vertically pointing in situ radars (described in Table 1 with corresponding index numbers). Comparison of in situ radar bright-band measurements and (b) concomitant colocated GPM-DPR bright-band height measurements within 100 km and 1 h. Measurements when the daily bright-band standard deviation at the in situ radar was <200 m are colored according to distance and time lag. Bright-band heights units are meters above sea level.

Table 2
Comparisons of Measured Bright-Band Height at Each In Situ Radar With Concomitant, Colocated GPM-DPR Bright-Band Height Measurements

		Radius $<$ 100 km time $<$ 1 h			Radius $<$ 100 km time $<$ 1 h standard deviation $<$ 200 m			Radius $<$ 50 km time $<$ 0.5 h standard deviation $<$ 200 m		
ID	Name	ε (m)	n	σ (m)	ε (m)	n	σ (m)	ε (m)	n	σ (m)
1	Forks	299.2	15	436.7	171.2	6	157.5	177.5	5	162.3
2	Astoria	304.0	19	498.0	96.6	8	97.4	31.8	3	31.7
3	Troutdale	511.9	14	715.9	144.3	5	91.7	40.8	2	24.3
3*	Troutdale*	465.2	16	674.5	139.4	7	109.3	77.7	3	55.9
4	Wasco	350.5	6	718.1	69.1	3	72.8	63.1	2	87.0
5	Boardman	88.4	5	68.7	88.4	5	68.7	124.9	2	73.2
6	Condon	245.5	3	203.8	245.5	3	203.8	202.3	3	268.8
7	Prineville	328.1	2	389.0	53.0	1	NA	NA	0	NA
8	North Bend	383.4	18	423.8	267.5	9	290.5	171.9	4	105.1
9	Happy Camp	393.0	21	593.0	299.3	6	151.4	103.6	1	NA
10	Shasta Dam	91.0	6	82.7	243.5	2	160.4	160.4	2	117.4
11	Chico	222.2	4	139.5	147.4	1	NA	NA	0	NA
12	Oroville	192.8	8	231.1	190.1	3	214.9	31.9	1	NA
13	Colfax	166.2	5	123.2	54.6	2	5.3	2.0	1	NA
14	New Exchequer	436.4	11	743.6	136.1	6	61.9	112.0	5	44.2
15	Pine Flat Dam	61.4	6	44.1	68.9	5	44.9	76.8	3	64.0
16	Visalia	189.9	4	117.9	189.9	4	117.9	149.8	2	71.2
17	Kernville	248.7	3	90.2	254.1	1	NA	NA	0	NA
18	San Bernardino	117.7	3	80.1	163.3	2	19.8	NA	0	NA
19	Santa Barbara	NA	0	NA	NA	0	NA	NA	0	NA
20	San Luis Res.	652.0	11	652.0	408.5	4	554.8	NA	0	NA
21	Saint Helena	270.7	1	NA	NA	0	NA	NA	0	NA
22	Middletown	396.0	8	715.3	157.0	4	77.8	190.0	2	106.5
23	Santa Rosa	216.7	10	317.5	72.3	4	23.6	73.8	2	24.1
24	Bodega Bay	240.9	6	472.1	73.0	2	82.3	43.5	2	0.9
25	Cazadero	304.1	10	511.7	44.3	4	45.5	82.4	2	40.6
26	Hopland	332.4	8	717.9	65.3	2	53.8	NA	0	NA
27	McKinleyville	166.6	12	135.5	100.8	6	71.3	76.2	2	54.6
		284.2	**235**	**380.6**	**151.7**	**105**	**118.9**	**99.6**	**49**	**78.3**

Note. Mean absolute error (ε), the number of records (n), and the standard deviation (σ) are given. The data correspond to Figure 4b. NA = not applicable. Bold values indicate column-averaged error, column total records, and column-averaged standard deviation. The asterisk indicates a the 915 MHz profiler at Troutdale, which also had a 449 MHz profiler (no asterisk).

TRMM-PR, proved capable of reproducing orographic precipitation gradients in various mountain regions over its lengthy temporal record (e.g., Anders et al., 2006). Given GPM-DPR's improved ability to measure solid-state precipitation, which is prevalent in the Sierra and Cascade Mountains during winter events (Serreze et al., 2001), it is likely that additional data collection in the future will augment the representation of regional precipitation patterns. While this section emphasizes the necessity for caution in interpreting GPM-DPR observations over regions of infrequent precipitation or topographic complexity, it should be noted that the manuscript's conclusions were not sensitive to the number of cross-track bins used.

3.2. Bright-Band Height

The layer at which precipitation transitions from rain to snow can be identified by an increase in radar reflectivity due to differences in the dielectric constant of ice and liquid water and the aggregation of ice particles as they descend and melt (Austin & Bemis, 1950; Hooper & Kippax, 1950). Identification of a radar bright band is important for discerning precipitation processes, which further influence reflectivity-derived precipitation rate estimates on account of differing drop-size distributions for bright-band and non-bright-band precipitation (Martner et al., 2008). Warm-type stratiform precipitation over Coastal California, which is driven by coalescence in shallow precipitating clouds, typically does not exhibit a radar bright band and is defined by smaller drop-size distributions, more numerous hydrometeors, and lighter precipitation rates than cold-type stratiform precipitation, which does typically exhibit a radar bright band and arises from ice processes in deep cloud layers associated with synoptic forcing (Martner et al., 2008). These differences may also lead to significant variability in accumulated precipitation between ARs, irrespective of moisture

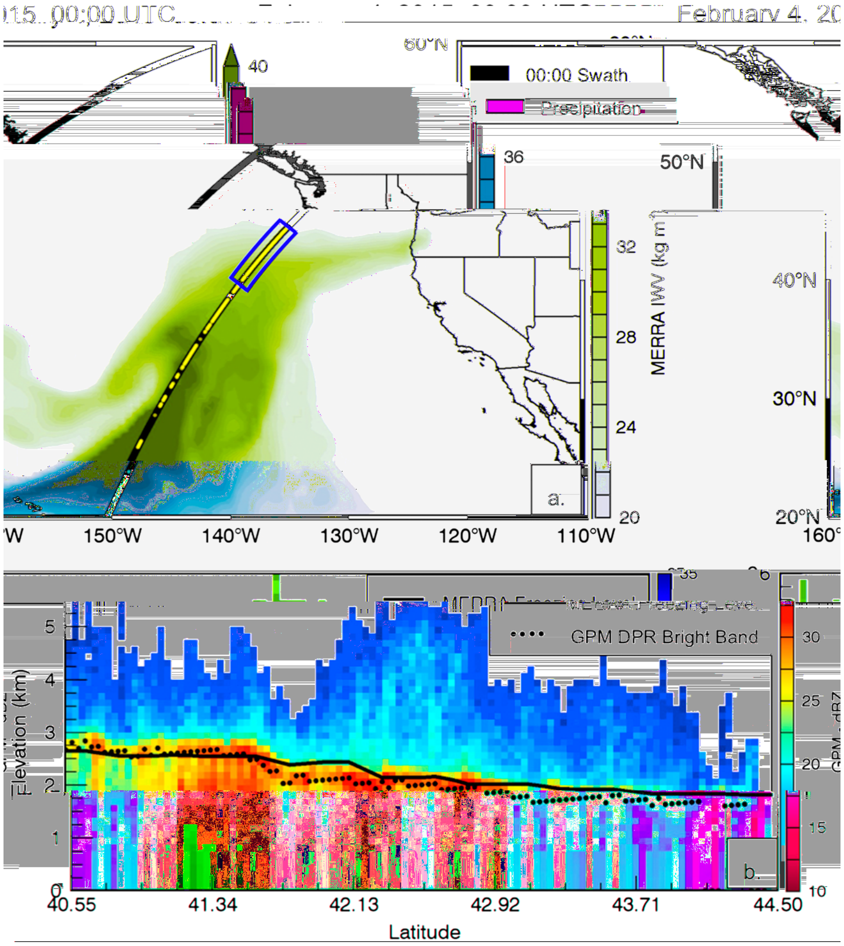

Figure 5. (a) A GPM-DPR swath through AR conditions on 4 February 2015 at 0:00 UTC and (b) the vertical profile of reflectivity from the Ka band along the center of the GPM-DPR swath subset within the red box in Figure 5a.

flux conditions (Martner et al., 2008; White et al., 2002). Given the importance of these processes, GPM-DPR bright-band measurements were compared with a network of 27 vertically pointing ground-based radars (described in section 2). The principal characteristics of the radars—coordinates, altitude, profiling frequency, installation data, and project name—are detailed in Table 1, and their locations, along with a reference map of the study region, are shown in Figure 4a.

GPM-DPR recorded a bright band within 100 km of one of the network's radars 241 times during the 2014–2017 study period. No single location accounted for more than 21 observations, though sites in the northern and coastal extents of the domain accounted for proportionally more observations due to the increased frequency of precipitation. A bright band was also observed at the colocated ground-based radar within 1 h of the satellite measurement in 235 of the 241 instances, indicating that false positive identifications of a bright band by GPM-DPR were uncommon. Additionally, GPM-DPR observations of precipitation exceeding 1 mm h^{-1} failed to identify an existing bright band only 16 times. GPM-DPR bright-band heights were compared with concomitant ground observations in Figure 4b. The different colored points in the scatterplot indicate increasingly stringent spatiotemporal thresholds that are meant to ensure that each sensor's measurements were based on samples of the same features. Mean differences between GPM-DPR bright-band height and individual ground-based radar sites, the number of observations, and the standard deviation of the mean differences are detailed in Table 2.

The mean absolute error of GPM-DPR bright-band heights relative to the ground network was 284 m for the 235 comparable instances, and the correlation was 0.59 ($p < 0.05$). The discrepancy between these is primarily attributable to rapid changes in bright-band height in the ground-based radars, which frequently occur

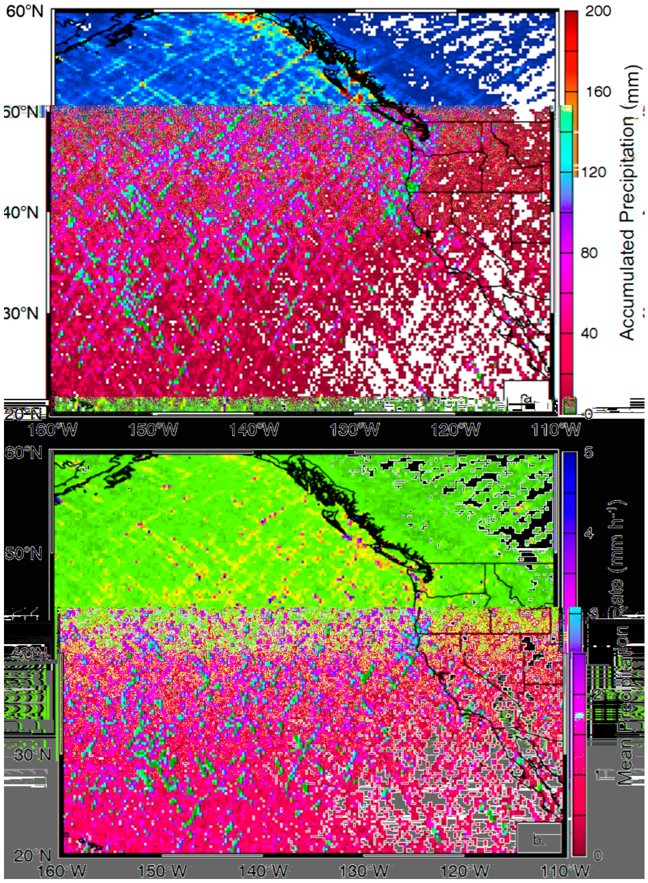

Figure 6. (a) Accumulated GPM-DPR precipitation during winter seasons 2014–2017 and (b) mean precipitation rate, binned at 0.25° latitude/longitude resolution.

during frontal passages, and can exhibit subhourly decreases in bright-band height of more than 1,000 m. Challengingly, precipitation also frequently occurs during frontal passages. Excluding instances in which the standard deviation of the ground-based radar's bright-band height for the date of the overpass exceeded 200 m (an empirically defined value intended to identify conditions that may lead to a comparison of measurements from different air masses) not only reduced the number of comparable overpasses to 105 but also reduced the mean error to 152 m and improved the correlation to 0.92. Further constraining the data to only compare measurements within a 50 km radius and 0.5 h of the radar observation decreased the sample size to 49, decreased the mean error to 100 m, and increased the correlation to 0.97. This error is smaller than the effective vertical resolution of the GPM-DPR data used in the study (125 m). GPM-DPR appears to be capable of identifying bright-band features and accurately estimating their elevation. Although the dense network of ground-based snow-level radars is unique to the West Coast, Matrosov et al. (2017) demonstrated significant agreement between these data and NEXRAD WSR-88D bright-band height estimates, indicating that a similar evaluation of GPM-DPR could be performed across much of the U.S. using this large network of operational radars.

4. GPM-DPR Over the Eastern North Pacific Ocean

4.1. GPM-DPR Oceanic Precipitation

An example GPM crossing of a landfalling AR over the eastern North Pacific Ocean on 4 February 2015, and the corresponding along-track reflectivity retrieval, is demonstrated in Figure 5. This is the same AR feature that is depicted in Figure 1, 4 days prior. The integrated water vapor (IWV) field, which identifies the position of the AR, was taken from MERRA-2 data for the corresponding time slice. In this particular case, precipitation was entirely confined to the plume of IWV greater than 20 mm, corresponding to AR conditions (Neiman et al., 2008; Ralph et al., 2004). The reflectivity profile for a 4° subset of the GPM swath, between 40.55 and 44.50°N, demonstrates an example bright-band retrieval, which characteristically decreased with increasing latitude (Matrosov, 2013) (Figure 5b). This particular swath demonstrates good agreement between the GPM-DPR bright-band and MERRA-2 freezing level, with the freezing level generally several hundred meters higher. The maximum precipitation rate of 9.74 mm h^{-1} (not shown) in this swath subset was found at 41.25°N, colocated with a maximum reflectivity of 35 dB*Z* and bright-band height of 2,618 m. The MERRA-2 time-averaged hourly precipitation amount for the corresponding grid point was 3.24 mm, and the MERRA-2 3-hourly instantaneous IWV was 31.4 mm. The mean bright-band height of this swath subset was 1956 m, the mean MERRA-2 freezing elevation was 2202 m, and the mean absolute difference was 282 m. The analyses presented in the remainder of this manuscript are based on the aggregation of precipitation and bright-band height statistics, similar to those presented in this example case, for all GPM-DPR retrievals within the study period.

GPM-DPR total measured winter precipitation and average precipitation rate (Figure 6) and the proportion of precipitation contributed by ARs (not shown) exhibited latitudinal dependence over the eastern North Pacific Ocean during the study period. The highest precipitation totals were generally found between 40° and 50°N, in a regime of frequent, moderate-intensity winter precipitation relative to the rest of the domain. Stratiform precipitation, as defined by the GPM-DPR classification method based on the slope of the ratio of Ku band and Ka band reflectivity, the intensity of reflectivity in the absence of a bright band, and the spatial distribution of reflectivity peaks (Awaka et al., 2016; Le & Chandrasekar, 2013a), accounted for 80.6% of total precipitation. Convection, which is also identified by GPM-DPR's precipitation classification module (Le & Chandrasekar, 2013a), accounted for the remainder. Stratiform was the dominant precipitation type in all

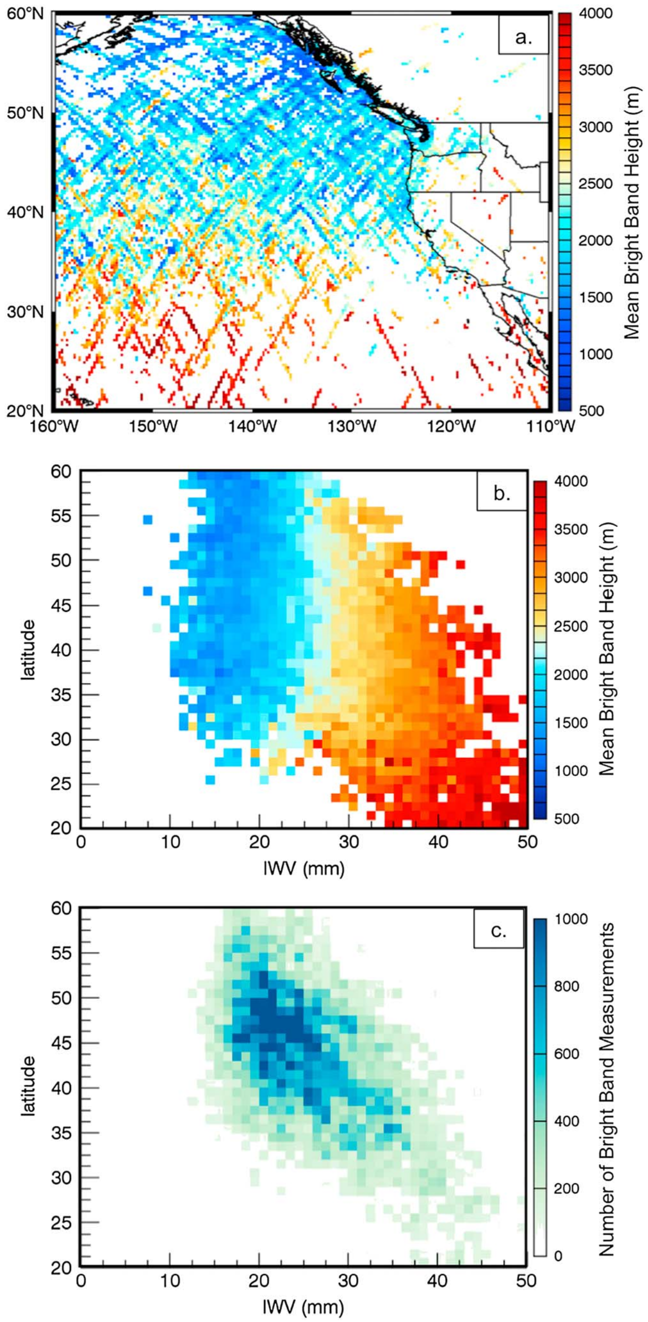

Figure 7. (a) Mean GPM-DPR bright-band height measurements for all overpasses that identified a bright band during the study period, binned at 0.25° latitude/longitude resolution. (b) Bright-band height binned by 1° latitude and 2 mm MERRA-2 IWV. (c) Total number of bright-band retrievals binned by 1° latitude and 2 mm MERRA-2 IWV.

regions except the southwestern portion of the domain, near Hawaii, which exhibited infrequent convection during non-AR periods (not shown). Bright-band precipitation accounted for 63% of total stratiform precipitation and nonbright band accounted for 37%. The mean precipitation rates for each category were 0.74 mm h^{-1} for stratiform nonbright band, 1.86 mm h^{-1} for stratiform bright band, and 2.47 mm h^{-1} for convective.

A catalog of AR events, based on the tracking algorithm defined by Rutz et al. (2014), was applied to investigate whether AR conditions affected precipitation amount or precipitation processes within the study domain. The AR catalog extends only until the end of 2015. During this period, 83% of stratiform bright-band precipitation occurred in AR conditions, compared to only 46% of non-bright-band stratiform precipitation, a statistically significant difference. Overall, 75% of GPM-identified precipitation within AR features was stratiform bright band. While individual AR features often exhibited both precipitation types, similar to findings from Matrosov (2013) that CloudSat-based study determined that the proportions of non-bright-band and bright-band precipitation were nearly equal within ARs. The discrepancy between studies likely arises due differences in each sensor's sensitivity range. CloudSat has an approximate precipitation threshold range between 0.02 and 5 mm h^{-1} (Stephens et al., 2010). By comparison, 5 mm h^{-1} is only the 65th percentile of measured GPM-DPR precipitation rates in this study. Since bright-band stratiform precipitation exhibited higher mean rain rates (Matrosov, 2013), it is possible that GPM-DPR is biased toward measuring bright-band precipitation and that Cloudsat is biased toward measuring non-bright-band precipitation. The proportions of each rain type were also temperature dependent (Matrosov, 2013; Ralph et al., 2004), indicating that latitude, time in the season, interannual variability, and synoptic conditions likely influenced these results.

4.2. GPM-DPR Oceanic Bright-Band Height

Example GPM-DPR bright-band height measurements within an AR in the eastern North Pacific on 3 February 2015 were demonstrated previously (Figure 5b). Here measured bright-band heights for all instances in which GPM-DPR exhibited a bright band during the study period were considered. Aggregated statistics from bright-band height retrievals exhibit strong latitudinal dependence over the study domain (Figure 7a). Mean bright-band height over oceanic portions of the domain decreased more than 1,000 m (from approximately 3,000 m to 2,000 m) between 30° and 50°N. Mean bright-band height also exhibited a statistically significant positive relationship with IWV (Figure 7b), indicating that the latitude dependence of mean bright-band height is influenced by the effect of the latitudinal temperature gradient on moisture content. Precipitation systems at lower latitudes of the domain were characteristically warmer and contain more water vapor, due to the Clausius Clapeyron relationship. Below 30°N, stratiform bright-band precipitation was observed relatively infrequently and only for MERRA-2 IWV values in excess of 30 mm (Figure 7c). Contrastingly, the most frequent stratiform bright-band precipitation retrievals occurred between 35° and 50°N and exhibited a steep gradient in mean bright-band height that depended upon moisture content. The standard deviation of bright-band height measurements in this middle-latitude range was notably large on account of the variability in temperature between individual AR events (not shown).

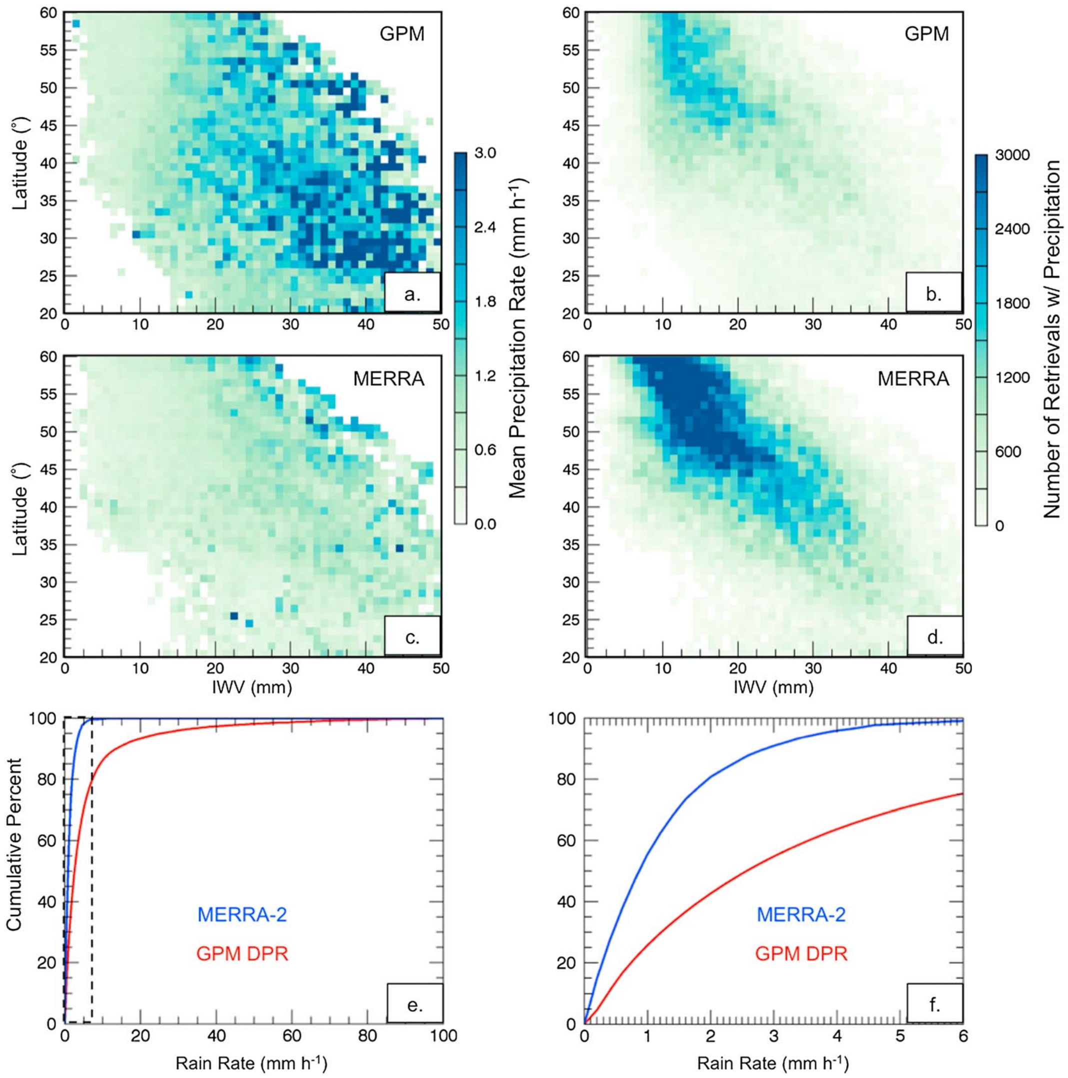

Figure 8. (a) GPM-DPR precipitation rate measurements for all overpasses within 1° latitude and 2 kg m^2 MERRA-2 IWV bins. (b) Total number of GPM-DPR samples with precipitation, (c) MERRA-2 precipitation rate, and (d) total number of GPM-DPR samples with colocated MERRA-2 precipitation. (e) Cumulative distribution function of oceanic precipitation in the study domain, according to rain rate, and (f) an enlarged view of the cumulative distribution function for rain rates less than 6 mm h^{-1}.

5. Comparison With Reanalysis

5.1. Comparison of GPM-DPR and MERRA-2 Precipitation

Comparisons of GPM-DPR precipitation with MERRA-2 equivalents yield insight about the sources of bias in each product over the study domain. AR conditions accounted for 69% of GPM-DPR precipitation and 60% of total MERRA-2 precipitation, inferring discrepancies in their frequency and intensity distributions. Excluding MERRA-2 precipitation rates below 0.2 mm h^{-1}, on account of GPM-DPR's minimum sensitivity, removed 21% of total MERRA-2 precipitation and increased the AR contribution to 65%. Subsequent comparisons between products used only MERRA-2 precipitation exceeding 0.2 mm h^{-1}; however, discrepancies in their distributions persisted. Scatterplots of the mean precipitation rate within 1° latitude × 2 mm precipitable water bins indicate that more intense but less frequent GPM-DPR precipitation was recorded in conditions with IWV $>$ 20 mm (Figures 8a–8d).

A cumulative frequency distribution plot comparing oceanic precipitation between MERRA-2 and GPM-DPR (Figures 8e and 8f) clearly demonstrates that low-intensity precipitation accounted for far more total precipitation in MERRA-2 than GPM-DPR. In fact, 10% of all GPM-DPR data were observed at precipitation rates that

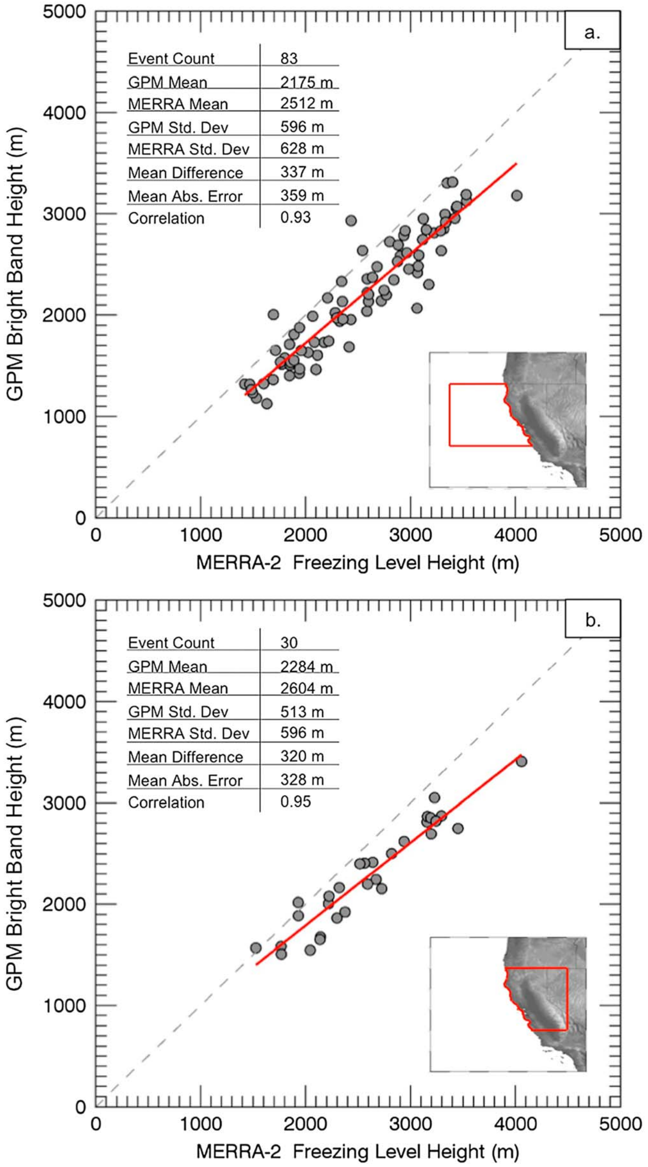

Figure 9. Scatterplot of along-track mean GPM-DPR bright-band height and mean MERRA-2 freezing level height for each event during the study period for (a) offshore and (b) onshore domains. The red line indicates the best fit linear relationship. The domains are shown in the red box within the map inset.

exceeded the highest value in MERRA-2, and 25% of GPM-DPR precipitation fell at rain rates above MERRA-2's 99th percentile. MERRA-2's comparative underestimation of precipitation rates in high precipitable water conditions at low-to-middle latitudes likely results from several factors, including the following: the comparison of mean grid-scale precipitation with instantaneous point observations (Wehner et al., 2010), well-known light precipitation biases in coarse-resolution models (Intergovernmental Panel on Climate Change, 2007), and GPM-DPR's difficulty measuring light precipitation (near or below its minimum sensitivity of ~12 dB*Z*). Unlike Stephens et al. (2010), who also demonstrated discrepancies between Cloudsat and global model precipitation distributions, the present study did not attempt to reconcile these differences through statistical upscaling or downscaling of the independent precipitation sources in order to achieve a direct comparison. Thus, differences shown here are important considerations regarding uncertainty in each data sources' precipitation distribution but are not intended to quantify error.

Discriminating between convective and stratiform precipitation, as identified by GPM-DPR (Awaka et al., 2016), further substantiates the origin of differences between products. MERRA-2 precipitation was evaluated based on the GPM-DPR precipitation classification. Stratiform (convective) precipitation accounted for 75% (25%) of GPM-DPR precipitation and colocated MERRA-2 precipitation accounted for 93% (7%) of the MERRA-2 along-track total. It is important to note that only 50% of along-track MERRA-2 precipitation was included in this analysis given that a GPM-DPR precipitation measurement was necessary to define precipitation type. The large difference in stratiform and convective rainfall between precipitation products is explained by an overestimation of precipitation by MERRA-2 during GPM-defined low-intensity non-bright-band stratiform precipitation and an underestimation of precipitation during moderate-to-high-intensity convective conditions. The lack of convective precipitation is partially explained by the inability of coarse-resolution models to explicitly resolve convection (Prein et al., 2015; Warner, 2011; Warner & Hsu, 2000). Importantly, non-bright-band stratiform precipitation was evenly distributed between AR and non-AR conditions, while AR conditions produced >83% of bright-band stratiform and >68% of convective precipitation in both GPM-DPR and MERRA-2. Thus, the increased proportion of light-intensity MERRA-2 precipitation in non-bright-band stratiform conditions decreased the overall contribution of ARs to total simulated oceanic precipitation, relative to GPM-DPR.

5.2. Comparison of GPM-DPR Bright-Band Height and MERRA-2 Freezing Level

MERRA-2 freezing level height and GPM-DPR bright-band height were compared to verify each product's representation of temperature in precipitating systems. MERRA-2 freezing level is defined as the height of the 0°C isotherm, which is typically several hundred meters above the observed bright band because the melting of frozen hydrometeors falling through the 0°C isotherm is not instantaneous (Houze, 1997; Leary & Houze, 1979; Minder & Kingsmill, 2013; Stewart et al., 1984). A case study comparison of GPM-DPR bright-band height measurements and colocated MERRA-2 freezing level height was shown in Figure 5b and discussed in section 4.2. Here similar analysis was applied for all GPM bright-band measurements near the Central and Northern California coast (Figure 9a, inset). The mean along-track GPM-DPR bright-band height and corresponding MERRA-2 freezing level height for all 83 valid winter overpasses had a mean bright-band height of 2175 m and mean MERRA-2 freezing elevation of 2,512 m, although the event-to-event variability was large. Despite a bright-band height range of more than 2,500 m and standard deviation of

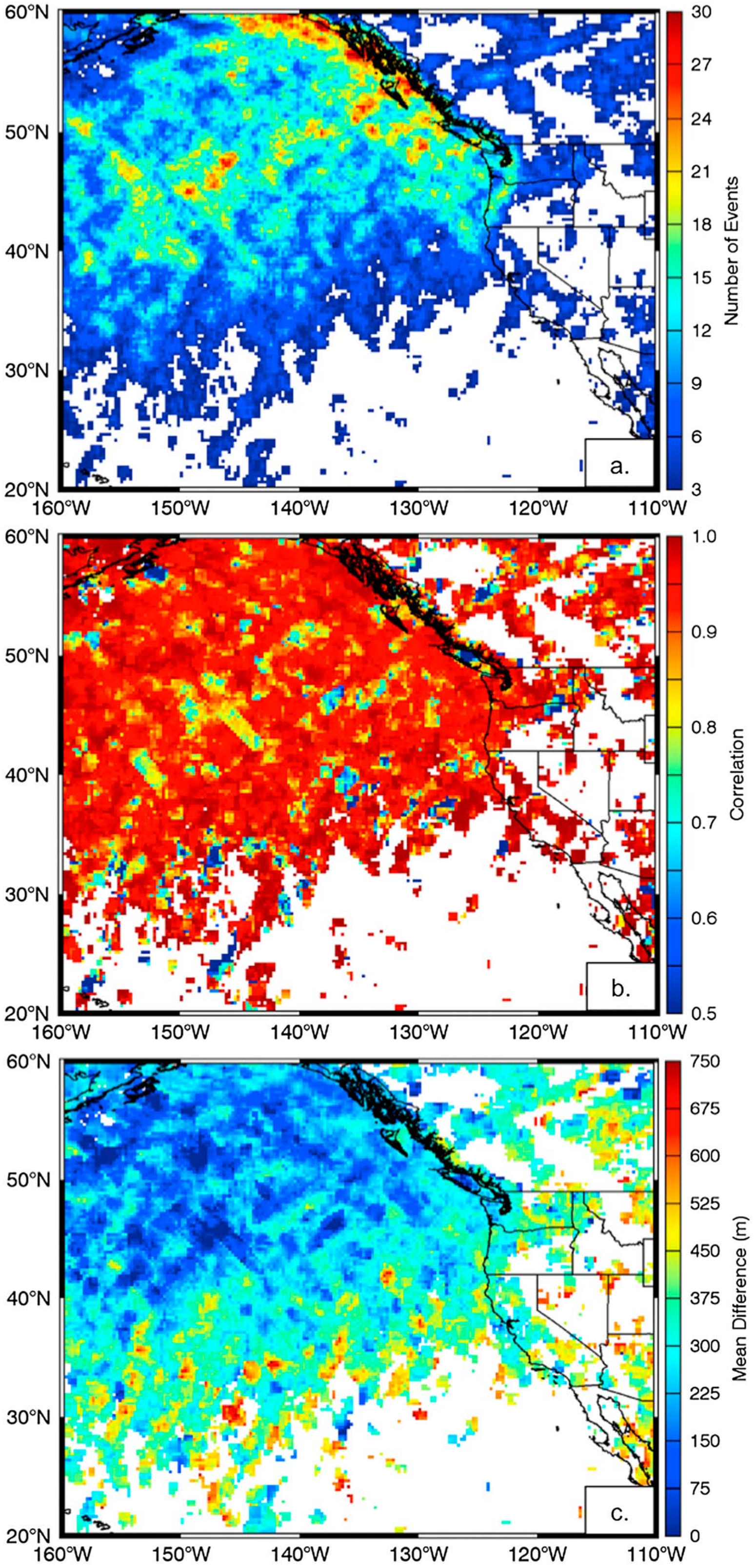

Figure 10. (a) Number of overpasses with a GPM-DPR bright-band measurement for all 1° × 1° bins with at least three valid measurements. (b) Correlation between the mean GPM-DPR bright-band height and concomitant mean MERRA-2 freezing level. (c) Average difference between GPM-DPR the mean bright-band heights and concomitant mean MERRA-2 freezing level.

~600 m, the correlation with MERRA-2 freezing level was 0.93, indicating exceptional agreement in capturing event-to-event temperature variability (Figure 9a). The mean absolute difference between bright-band height and freezing level height was 356 m, with larger variance in events with higher bright-band heights. Results of comparisons over the onshore domain were not appreciably different (Figure 9b).

Performing similar comparisons within 1° × 1° grid boxes covering the entire study domain, the mean correlation between MERRA-2 freezing level height and all GPM-DPR overpasses was 0.93. High correlations were relatively uniform across the domain (Figure 10b), confirming that GPM-DPR measurements were sensitive to the primary drivers of freezing level height variability, including the seasonal cycle, latitude, and synoptic weather events. The mean difference between bright-band height and colocated MERRA-2 freezing level height for those overpasses was −288 m, which agrees with findings of an approximately −300 m difference between airborne measurements of bright-band height and freezing level height within maritime stratiform precipitation off the coast of California (Stewart et al., 1984; White et al., 2002). The difference between MERRA-2 and GPM-DPR varies by latitude, with larger differences south of 40°N and for higher precipitable water values (Figure 10c). Previous studies have also found that differences increase at lower latitude (Houze, 1997; Harris et al., 2000; Shin et al., 2000). These results demonstrate that GPM-DPR captures event-to-event freezing level variability with excellent skill and infer that its measurements could be used to independently observe variability and trends in the temperature characteristics of ARs over the satellite's lifetime. GPM-DPR bright-band height will additionally benefit validation of freezing level initial conditions and forecasts over the ocean and improve understanding of the offset between forecasted freezing level and observed snow level in the western United States (White et al., 2010). These advancements have the potential to significantly improve the skill of flood forecasting and hazard prediction associated with ARs (Neiman et al., 2014).

6. Conclusions

Precipitation over midlatitude oceans is not well measured or simulated (Stephens et al., 2010) and is an important source of uncertainty in the simulation of global water and energy fluxes in climate models (L'Ecuyer et al., 2015; include (Li et al., 2008) reference). Decades of passive infrared and microwave satellite observations over the eastern North Pacific Ocean have demonstrated that extratropical cyclones, and their associated atmospheric river (AR) features, are the primary driver of regional precipitation (Ralph et al., 2004). However, advancing understanding of precipitation processes in this region requires improved observations (e.g., Matrosov, 2013; Stephens et al., 2010). In this research, measurements of AR precipitation rates, microphysical processes, and freezing level from the Dual-Frequency Precipitation Radar (DPR) on board the Global Precipitation Measurement (GPM; Hou et al., 2014) satellite were evaluated relative to in situ observations and reanalyses during winter seasons 2014–2017.

GPM-DPR did not effectively reproduce the observed spatial patterns of precipitation accumulation over the western United States, due to sampling frequency and its minimum sensitivity. Accounting for these limitations, distributions of GPM-DPR precipitation measurements were evaluated over the eastern North Pacific Ocean and demonstrated that ARs accounted for nearly 70% of measured precipitation over the study period. These observations identified moderate- to high-intensity precipitation over the eastern North Pacific Ocean that was generally absent in global model simulation. MERRA-2 precipitation rates below the minimum sensitivity of GPM-DPR accounted for a 20% increase in total precipitation, and 25% of radar-derived precipitation rates were greater than the 99th percentile precipitation rate in reanalyses. Comparison of GPM-DPR with reanalyses further illuminated discrepancies between the proportions of non-bright-band stratiform, bright-band stratiform, and convective precipitation, which underscore the propensity of reanalyses to overestimate light precipitation and underestimate heavy precipitation. Notably, the higher proportion of low-intensity MERRA-2 precipitation in non-bright-band stratiform conditions diminished the contribution of ARs to total simulated oceanic precipitation by 10%, relative to GPM-DPR.

GPM-DPR also demonstrated utility in providing an accurate and independent measurement of AR freezing level height. Comparison of GPM-DPR-derived bright-band height with in situ radar in cold-type stratiform conditions exhibited a mean absolute error that was smaller than the effective resolution of the satellite product, and comparison with reanalysis freezing level height demonstrated exceptional agreement in event-to-event variability over the entire study domain. These results additionally indicate that GPM-DPR is potentially useful for independently investigating interannual precipitation and temperature variability in oceanic precipitating systems.

Diagnosing inconsistencies between satellite measurements and reanalyses lends perspective to precipitation and temperature biases in global models. This is necessary for interpreting model-based estimates of future AR characteristics and impacts (e.g., Dettinger, 2011; Guan & Waliser, 2017; Ralph et al., 2016; Warner et al., 2015), reducing uncertainty in numerical weather prediction forecasts (Okamoto et al., 2016; Ralph et al., 2010) and constraining simulated global moisture and energy budgets (L'Ecuyer et al., 2015). Although GPM-DPR exhibited several important limitations, chiefly related to sampling frequency and minimum reflectivity sensitivity, it is clear that the advanced satellite product yields tremendous benefit for reducing the data gap over the global oceans and supplementing current understanding of precipitation processes in ARs.

Acknowledgments
This research was supported by the National Aeronautics and Space Administration (NASA) grant NNX14AD77G. Any opinions, findings, and conclusions or recommendations expressed in this publication are those of the authors and do not necessarily reflect the views of NASA. The MERRA-2 data used in this research were developed by NASA's Global Modeling and Assimilation Office (GMAO) and disseminated by the Goddard Earth Sciences Data and Information Services Center (GES DISC). Observational GPM data sets are made available through a joint collaboration between JAXA and NASA, with data access also made available by GES DISC. Radar profiler data were provided by the NOAA/OAR/ESRL PSD, Boulder, Colorado, USA, from their website at www.esrl.noaa.gov/psd/. PRISM data are provided by the PRISM Climate Group at Oregon State University and are available through www.prism.oregonstate.edu.

References

Adler, R. F., Huffman, G. J., Chang, A., Ferraro, R., Xie, P.-P., Janowiak, J., … Nelkin, E. (2003). The version-2 Global Precipitation Climatology Project (GPCP) monthly precipitation analysis (1979–present). *Journal of Hydrometeorology*, *4*(6), 1147–1167. https://doi.org/10.1175/1525-7541(2003)004%3C1147:TVGPCP%3E2.0.CO;2

Anders, A. M., Roe, G. H., Hallet, B., Montgomery, D. R., Finnegan, N. J., & Putkonen, J. (2006). Spatial patterns of precipitation and topography in the Himalaya. *Geological Society of America*, *398*, 39–53.

Austin, P. M., & Bemis, A. C. (1950). A quantitative study of the "bright band" in radar precipitation echoes. *Journal of Meteorology*, *7*(2), 145–151. https://doi.org/10.1175/1520-0469(1950)007%3C0145:AQSOTB%3E2.0.CO;2

Awaka, J., Le, M., Chandrasekar, V., Yoshida, N., Higashiuwatoko, T., Kubota, T., & Iguchi, T. (2016). Rain type classification algorithm module for GPM dual-frequency precipitation radar. *Journal of Atmospheric and Oceanic Technology*, *33*(9), 1887–1898. https://doi.org/10.1175/JTECH-D-16-0016.1

California Department of Water Resources (2016). Hydroclimate report water year 2015. Memorandum report.

Daly, C., Neilson, R. P., & Phillips, D. L. (1994). A statistical-topographic model for mapping climatological precipitation over mountainous terrain. *Journal of Applied Meteorology*, *33*(2), 140–158. https://doi.org/10.1175/1520-0450(1994)033%3C0140:ASTMFM%3E2.0.CO;2

Dettinger, M. (2011). Climate change, atmospheric rivers, and floods in California—A multimodel analysis of storm frequency and magnitude changes. *Journal of the American Water Resources Association*, *47*(3), 514–523. https://doi.org/10.1111/j.1752-1688.2011.00546.x

Dettinger, M. (2013). Atmospheric rivers as drought busters on the U.S. West Coast. *Journal of Hydrometeorology*, *14*(6), 1721–1732. https://doi.org/10.1175/JHM-D-13-02.1

Dettinger, M., Redmond, K., & Cayan, D. (2004). Winter orographic precipitation ratios in the Sierra Nevada—Large-scale atmospheric circulations and hydrologic consequences. *Journal of Hydrometeorology*, *5*(6), 1102–1116. https://doi.org/10.1175/JHM-390.1

Gimeno, L., Raquel, N., Vazquez, M., & Lavers, D. A. (2014). Atmospheric rivers: A mini-review. *Frontiers in Earth Science*, *2*, 1–6.

Guan, B., & Waliser, D. E. (2017). Atmospheric rivers in 20 year weather and climate simulations: A multi-model, global evaluation. *Journal of Geophysical Research: Atmospheres*, *122*, 5556–5581. https://doi.org/10.1002/2016JD026174

Hamada, A., & Takaybu, Y. N. (2016). Improvements in detection of light precipitation with the Global Precipitation Measurement Dual-Frequency Precipitation Radar (GPM-DPR). *Journal of Atmospheric and Oceanic Technology*, *33*, 653–667.

Harris, G. N. Jr., Bowman, K. P., & Shin, D.-B. (2000). Comparison of freezing-level altitudes from the NCEP reanalysis with TRMM precipitation radar bright band data. *Journal of Climate*, *13*(23), 4137–4148. https://doi.org/10.1175/1520-0442(2000)013%3C4137:COFLAF%3E2.0.CO;2

He, M., Russo, M., & Anderson, M. (2017). Hydroclimatic characteristics of the 2012–2015 California Drought from an operational perspective. *Climate*, *5*(1). https://doi.org/10.3390/cli5010005

Hirose, M., Shimizu, S., Oki, R., Iguchi, T., Short, D. A., & Nakamura, K. (2012). Incidence-angle dependency of TRMM PR rain estimates. *Journal of Atmospheric and Oceanic Technology*, *29*(2), 192–206. https://doi.org/10.1175/JTECH-D-11-00067.1

Hooper, J. E. N., & Kippax, A. A. (1950). The bright band, a phenomenon associated with radar echoes from falling rain. *Quarterly Journal of the Royal Meteorological Society*, *76*(328), 125–132. https://doi.org/10.1002/qj.49707632803

Hou, A. Y., Kakar, R. K., Neeck, S. A., Azarbarzin, A., Kummerow, C. D., Kojima, M., … Iguchi, T. (2014). The global precipitation measurement mission. *Bulletin of the American Meteorological Society*, *95*(5), 701–722. https://doi.org/10.1175/BAMS-D-13-00164.1

Houze, R. A. Jr. (1997). Stratiform precipitation in regions of convection: A meteorological paradox? *Bulletin of the American Meteorological Society*, *78*(10), 2179–2196. https://doi.org/10.1175/1520-0477(1997)078%3C2179:SPIROC%3E2.0.CO;2

Houze, R. A., Houze, R. A. Jr., McMurdie, L. A., Petersen, W. A., Schwaller, M. R., Baccus, W., … Barnes, H. C. (2017). The Olympic Mountains Experiment (OLYMPEX). *Bulletin of the American Meteorological Society*, *98*(10), 2167–2188. https://doi.org/10.1175/BAMS-D-16-0182.1

Huffman, G. J., Bolvin, D. T., Nelkin, E. J., Wolff, D. B., Adler, R. F., Gu, G., … Stocker, E. F. (2007). The TRMM multisatellite precipitation analysis (TMPA): Quasi-global, multiyear, combined-sensor precipitation estimates at fine scales. *Journal of Hydrometeorology*, *8*(1), 38–55. https://doi.org/10.1175/JHM560.1

Iguchi, T., Shinta, S., Menghini, R., Yoshida, N., Awaka, J., Le, M., … Kubota, T. (2010). *GPM/DPR Level-2 algorithm theoretical basis document* (p. 68). Retrieved from https://pps.gsfc.nasa.gov/atbd.html

Intergovernmental Panel on Climate Change (2007). In S. Solomon, et al. (Eds.), *Climate models and their evaluation. Climate change, 2007: The physical science basis. Contribution of Working Group I to the Fourth Assessment Report of the Intergovernmental Panel on Climate Change* (pp. 627–629). Cambridge, UK: Cambridge University Press.

Kingston, D. G., Lavers, D. A., & Hannah, D. M. (2016). Floods in the Southern Alps of New Zealand: The importance of atmospheric rivers. *Hydrological Processes*, *30*(26), 5063–5070. https://doi.org/10.1002/hyp.10982

Kubota, T., Iguchi, T., Kojima, M., Liao, L., Masaki, T., Hanado, H., … Oki, R. (2016). A statistical method for reducing sidelobe clutter for the Ku-band precipitation radar on board the GPM Core Observatory. *Journal of Atmospheric and Oceanic Technology*, *33*(7), 1413–1428. https://doi.org/10.1175/JTECH-D-15-0202.1

L'Ecuyer, T. L., Beaudoing, H. K., Rodell, M., Olson, W., Lin, B., Kato, S., … Hilburn, K. (2015). The observed state of the energy budget in the early twenty-first century. *Journal of Climate*, *28*, 8320–8346.

Lavers, D. A., & Villarini, G. (2013). The nexus between atmospheric rivers and extreme precipitation across Europe. *Geophysical Research Letters*, *40*(12), 3259–3264. https://doi.org/10.1002/grl.50636

Le, M., & Chandrasekar, V. (2013a). Precipitation type classification method for Dual-Frequency Precipitation Radar (DPR) onboard the GPM. *Transactions on Geoscience and Remote Sensing*, *51*(3), 1784–1790. https://doi.org/10.1109/TGRS.2012.2205698

Le, M., & Chandrasekar, V. (2013b). Hydrometeor profile characterization method for dual-frequency precipitation radar onboard the GPM. *Transactions on Geoscience and Remote Sensing*, *51*, 3648–3658.

Leary, C. A., & Houze, R. A. Jr. (1979). The structure and evolution of convection in a tropical cloud cluster. *Journal of the Atmospheric Sciences*, *36*(3), 437–457. https://doi.org/10.1175/1520-0469(1979)036%3C0437:TSAEOC%3E2.0.CO;2

Li, J.-L., Waliser, D., Woods, C., Teixeira, J., BAcmeister, J., Chern, J., … Köhler, M. (2008). Comparisons of satellites liquid water estimates to ECMWF and GMAO analyses, 20th century IPCC AR4 climate simulations, and GCM simulations. *Geophysical Research Letters*, *35*(19), L19710. https://doi.org/10.1029/2008GL035427

Martner, E. B., Yuter, S. E., White, A. B., Matrosov, S. Y., Kingsmill, D. E., & Ralph, F. M. (2008). Raindrop size distributions and rain characteristics in California coastal rainfall for periods without a radar bright band. *Journal of Hydrometeorology*, *9*(3), 408–425. https://doi.org/10.1175/2007JHM924.1

Matrosov, S. Y. (2007). Potential for attenuated-based estimations of rainfall rate from CloudSat. *Geophysical Research Letters*, *34*(5), L05817. https://doi.org/10.1029/2006GL029161

Matrosov, S. Y. (2013). Characteristics of landfalling atmospheric rivers inferred from satellite observations over the eastern North Pacific Ocean. *Monthly Weather Review*, *141*(11), 3757–3768. https://doi.org/10.1175/MWR-D-12-00324.1

Matrosov, S. Y., Cifelli, R., White, A., & Coleman, T. (2017). Snow-level estimates using operational polarimetric weather radar measurements. *Journal of Hydrometeorology*, *18*(4), 1009–1019. https://doi.org/10.1175/JHM-D-16-0238.1

Minder, J. R., & Kingsmill, D. E. (2013). Mesoscale variations of the atmospheric snow line over the northern Sierra Nevada: Multiyear statistics, case study, and mechanisms. *Journal of the Atmospheric Sciences*, *70*(3), 916–938. https://doi.org/10.1175/JAS-D-12-0194.1

Molod, A., Takacs, L., Suarez, M., & Bacmeister, J. (2015). Development of the GEOS-5 atmospheric general circulation model: Evolution from MERRA-2 to MERRA2. *Geoscientific Model Development*, *8*(5), 1339–1356. https://doi.org/10.5194/gmd-8-1339-2015

Neiman, P. J., Gottas, D. J., White, A. B., Schick, L. J., & Ralph, F. M. (2014). The use of snow-level observations derived from vertically profiling radars to assess hydrometeorological characteristics and forecasts over Washington's Green River basin. *Journal of Hydrometeorology*, *15*(6), 2522–2541. https://doi.org/10.1175/JHM-D-14-0019.1

Neiman, P. J., Ralph, F. M., Wick, G. A., Lundquist, J., & Dettinger, M. D. (2008). Meteorological characteristics and overland precipitation impacts of atmospheric rivers affecting the West Coast of North America based on eight years of SSM/I satellite observations. *Journal of Hydrometeorology*, *9*(1), 22–47. https://doi.org/10.1175/2007JHM855.1

Okamoto, K., Aonashi, K., Kubota, T., & Tashima, T. (2016). Experimental assimilation of the GPM Core Observatory DPR reflectivity profiles for Typhoon Halong (2014). *Monthly Weather Review*, *144*(6), 2307–2326. https://doi.org/10.1175/MWR-D-15-0399.1

Prein, A. F., Langhans, W., Fosser, G., Ferrone, A., Ban, N., Goergen, K., … Leung, R. (2015). A review on regional convection-permitting climate modeling: Demonstrations, prospects, and challenges. *Reviews of Geophysics*, *53*(2), 323–361. https://doi.org/10.1002/2014RG000475

Ralph, F., Dettinger, M., Lavers, D., Gorodetskaya, I., Martin, A., Viale, M., … Cordeira, J. (2017). Atmospheric rivers emerge as a global science and applications focus. *Bulletin of the American Meteorological Society*, *98*, 1969–1973. https://doi.org/10.1175/BAMS-D-16-0262.1

Ralph, F. M., Neiman, P. J., & Wick, G. A. (2004). Satellite and CALJET aircraft observations of atmospheric rivers over the eastern North Pacific Ocean during the winter of 1997/98. *Monthly Weather Review*, *132*(7), 1721–1745. https://doi.org/10.1175/1520-0493(2004)132%3C1721:SACAOO%3E2.0.CO;2

Ralph, F. M., Prather, K. A., Cayan, D., Spackman, J. R., DeMott, P., Dettinger, M., … Intrieri, J. (2016). CalWater field studies designed to quantify the roles of atmospheric rivers and aerosols in modulating U.S. West Coast precipitation in a changing climate. *Bulletin of the American Meteorological Society*, *97*, 1209–1228. https://doi.org/10.1175/BAMS-D-14-00043.1

Ralph, F. M., Sukovich, E., Reynolds, D., Dettinger, M., Weagle, S., Clark, W., & Neiman, P. J. (2010). Assessment of extreme quantitative precipitation forecasts and development of regional extreme event thresholds using data from HMT-2006 and COOP observers. *Journal of Hydrometeorology*, *11*, 1288–1306.

Rienecker, M. M., Suarez, M. J., Gelaro, R., Todling, R., Bacmeister, J., Liu, E., … Woollen, J. (2011). MERRA: NASA's modern-era retrospective analysis for research and applications. *Journal of Climate*, *24*(14), 3624–3648. https://doi.org/10.1175/JCLI-D-11-00015.1

Roe, G. H. (2005). Orographic precipitation. *Annual Review of Earth and Planetary Sciences*, *33*(1), 645–671. https://doi.org/10.1146/annurev.earth.33.092203.122541

Rutz, J. J., Steenburgh, W. J., & Ralph, F. M. (2014). Climatological characteristics of atmospheric rivers and their inland penetration over the western United States. *Monthly Weather Review*, *142*(2), 905–921. https://doi.org/10.1175/MWR-D-13-00168.1

Serreze, M. C., Clark, M. P., & Frei, A. (2001). Characteristics of large snowfall events in the montane western United States as examined using snowpack telemetry (SNOTEL) data. *Water Resources Research*, *37*(3), 675–688. https://doi.org/10.1029/2000WR900307

Shin, D.-B., North, G. R., & Bowman, K. P. (2000). A summary of reflectivity profiles from the first year of TRMM radar data. *Journal of Climate*, *13*(23), 4072–4086. https://doi.org/10.1175/1520-0442(2000)013%3C4072:ASORPF%3E2.0.CO;2

Skofronick-Jackson, G., Petersen, W. A., Berg, W., Kidd, C., Stocker, E. F., Kirschbaum, D. B., … Wilheit, T. (2016). The Global Precipitation Measurement (GPM) mission for science and society. *Bulletin of the American Meteorological Society*, *98*(8), 1679–1695. https://doi.org/10.1175/BAMS-D-15-00306.1

Stephens, G. L., L'Ecuyer, T., Forbes, R., Gettlemen, A., Golaz, J.-C., Bodas-Salcedo, A., … Haynes, J. (2010). Dreary state of precipitation in global models. *Journal of Geophysical Research*, *115*, D24211. https://doi.org/10.1029/2010JD014532

Stephens, G. L., Vane, D. G., Boain, R. J., Mace, G. G., Sassen, K., Wang, Z., … the CloudSat Science Team (2002). The CloudSat mission and the A-train. A new dimension of space-based observations of clouds and precipitation. *Bulletin of the American Meteorological Society*, *83*(12), 1771–1790. https://doi.org/10.1175/BAMS-83-12-1771

Stewart, R., Marwitz, J., Pace, J., & Carbone, R. (1984). Characteristics through the melting layer of stratiform clouds. *Journal of the Atmospheric Sciences*, *41*(22), 3227–3237. https://doi.org/10.1175/1520-0469(1984)041%3C3227:CTTMLO%3E2.0.CO;2

Viale, M., & Nuñez, M. N. (2011). Climatology of Winter Orographic Precipitation over the Subtropical Central Andes and Associated Synoptic and Regional Characteristics. *Journal of Hydrometeorology*, *12*(4), 481–507.

Warner, M. D., Mass, C. F., & Salathe, E. P. Jr. (2015). Changes in winter atmospheric rivers along the North American West Coast in CMIP5 climate models. *Journal of Hydrometeorology*, *16*(1), 118–128. https://doi.org/10.1175/JHM-D-14-0080.1

Warner, T. T. (2011). *Numerical weather and climate prediction* (pp. 129–139). New York: Cambridge University Press.

Warner, T. T., & Hsu, H. (2000). Nested-model simulation of moist convection: The impact of coarse-grid parameterized convection on fine-grid resolved convection. *Monthly Weather Review*, *128*(7), 2211–2231. https://doi.org/10.1175/1520-0493(2000)128%3C2211:NMSOMC%3E2.0.CO;2

Wehner, F., Smith, R., Bala, G., & Duffy, P. (2010). The effect of horizontal resolution on simulation of very extreme US precipitation events in a global atmosphere model. *Climate Dynamics*, *34*(2-3), 241–247. https://doi.org/10.1007/s00382-009-0656-y

White, A. B., Anderson, M. L., Dettinger, M. D., Ralph, F. M., Hinojosa, A., Cayan, D. R., … Coleman, T. (2013). A 21st century California observing network for monitoring extreme weather events. *Journal of Atmospheric and Oceanic Technology*, *30*(8), 1585–1603. https://doi.org/10.1175/JTECH-D-12-00217.1

White, A. B., Gottas, D. J., Henkel, A. F., Neiman, P. J., Ralph, F. M., & Gutman, S. I. (2010). Developing a performance measure for snow-level forecasts. *Journal of Hydrometeorology*, *11*(3), 739–753. https://doi.org/10.1175/2009JHM1181.1

White, A. B., Gottas, D. J., Strem, E. T., Ralph, F. M., & Neiman, P. J. (2002). Automated bright band height detection algorithm for use with Doppler radar spectral moments. *Journal of Atmospheric and Oceanic Technology*, *19*(5), 687–697. https://doi.org/10.1175/1520-0426(2002)019%3C0687:AABHDA%3E2.0.CO;2

Zhu, Y., & Newell, R. (1998). A proposed algorithm for moisture fluxes from atmospheric rivers. *Monthly Weather Review*, *126*(3), 725–735. https://doi.org/10.1175/1520-0493(1998)126%3C0725:APAFMF%3E2.0.CO;2